

Disease severity in a mouse model of ataxia telangiectasia is modulated by the DNA damage checkpoint gene *Hus1*

Gabriel Balmus¹, Min Zhu¹, Sucheta Mukherjee¹, Amy M. Lyndaker¹, Kelly R. Hume¹, Jaesung Lee², Mark L. Riccio³, Anthony P. Reeves², Nathan B. Sutter⁴, Drew M. Noden¹, Rachel M. Peters¹ and Robert S. Weiss^{1,*}

¹Department of Biomedical Sciences, ²School of Electrical and Computer Engineering, ³Cornell Institute for Biotechnology and Life Science Technologies and ⁴Department of Clinical Sciences, Cornell University, Ithaca, NY 14853, USA

Received February 14, 2012; Revised and Accepted May 2, 2012

The human genomic instability syndrome ataxia telangiectasia (A-T), caused by mutations in the gene encoding the DNA damage checkpoint kinase ATM, is characterized by multisystem defects including neurodegeneration, immunodeficiency and increased cancer predisposition. ATM is central to a pathway that responds to double-strand DNA breaks, whereas the related kinase ATR leads a parallel signaling cascade that is activated by replication stress. To dissect the physiological relationship between the ATM and ATR pathways, we generated mice defective for both. Because complete ATR pathway inactivation causes embryonic lethality, we weakened the ATR mechanism to different degrees by impairing HUS1, a member of the 911 complex that is required for efficient ATR signaling. Notably, simultaneous ATM and HUS1 defects caused synthetic lethality. *Atm/Hus1* double-mutant embryos showed widespread apoptosis and died mid-gestationally. Despite the underlying DNA damage checkpoint defects, increased DNA damage signaling was observed, as evidenced by H2AX phosphorylation and p53 accumulation. A less severe *Hus1* defect together with *Atm* loss resulted in partial embryonic lethality, with the surviving double-mutant mice showing synergistic increases in genomic instability and specific developmental defects, including dwarfism, craniofacial abnormalities and brachymesophalangy, phenotypes that are observed in several human genomic instability disorders. In addition to identifying tissue-specific consequences of checkpoint dysfunction, these data highlight a robust, cooperative configuration for the mammalian DNA damage response network and further suggest *HUS1* and related genes in the ATR pathway as candidate modifiers of disease severity in A-T patients.

INTRODUCTION

Ataxia telangiectasia (A-T, OMIM #208900) is a hereditary genomic instability syndrome caused by loss of function mutations in *ATM*, which encodes a protein kinase involved in the cellular DNA damage response (DDR) (1). A-T is characterized by progressive cerebellar ataxia, oculocutaneous telangiectasias, immunodeficiency, infertility, increased cancer incidence and radiation hypersensitivity. These clinical manifestations are the consequence of failed responses to DNA

double-strand breaks (DSB) that arise spontaneously or as programmed developmental events. Rare patients with atypical manifestation of the disease have been described and referred to as 'A-T variants'. One such variant, termed A-T_{Fresno}, combines typical A-T phenotypes with microcephaly and mental retardation, making it among the most severe A-T forms known (2).

ATM normally functions as the main component of one of the cellular DNA damage checkpoint pathways that detect aberrant DNA structures and coordinate DNA repair with cell cycle

*To whom correspondence should be addressed at: Department of Biomedical Sciences, Cornell University, T2-006C Veterinary Research Tower, Ithaca, New York 14853, USA. Tel: +1 6072534443; Fax: +1 6072534212; Email: rsw26@cornell.edu

progression. Checkpoint mechanisms are part of a broader DDR that protects genomic integrity and ensures normal development, tissue homeostasis and cancer-free survival (3). In response to DSB, the ATM kinase undergoes a transition from inactive dimer to active, auto-phosphorylated monomer and then phosphorylates numerous substrates involved in signaling transduction and downstream effector functions, including H2AX, CHK2 and p53. A second checkpoint pathway, organized around the related kinase ATR, responds to a wide variety of lesions, including bulky DNA adducts and DNA crosslinks, as well as processed DSB. Activated ATR phosphorylates CHK1 and other targets, promoting fork stabilization, inhibition of late origin firing and stimulation of DNA repair (4). Critical for ATR activation is the RAD9–RAD1–HUS1 (911) complex, a PCNA-like clamp that is loaded onto damage sites and recruits the ATR activator TOPBP1 (5). Importantly, the 911 complex additionally has direct roles in regulating base excision repair, translesion DNA synthesis and apoptotic signaling (6). The genes encoding the 911 complex, like all ATR pathway core components, are essential for organismal survival (7–9). Partial *ATR* impairment in humans leads to Seckel syndrome (SCKL1, OMIM #210600), an autosomal recessive disorder characterized by proportional dwarfism, microcephaly, craniofacial abnormalities and mental retardation (10).

Owing to their distinct componentry and activation by different types of genome damage, the ATM and ATR pathways initially were thought to function as independent, separable mechanisms. However, aberrant DNA structures often engage both pathways to some extent, and there is substantial biochemical crosstalk between the pathways (4). A full appreciation of these interactions in vertebrates has been hampered by a lack of suitable genetic tools. Although *Atm*-deficient mice are viable and show many A-T phenotypes (11–13), the severe phenotypes associated with ATR pathway impairment have been an impediment to understanding the biological significance of the interplay between the ATM and ATR pathways. In this study, we overcome this limitation with an *Hus1* allelic series in which null (*Hus1*^{Δ1n}) or wild-type (*Hus1*⁺) alleles are used in combination with a hypomorphic (*Hus1*^{neo}) allele that expresses *Hus1* at ~40% of the wild-type level (14). *Hus1*^{neo/Δ1n} mice, which have the lowest *Hus1* expression in the series, are born at expected frequencies and appear grossly normal but are incapable of proper genome maintenance as evidenced by increased spontaneous GIN and hypersensitivity to exogenous genotoxins (14). By combining the *Hus1* allelic series with targeted *Atm* deletion, we identify an essential cooperative relationship between ATM and HUS1 during embryonic development and in specific adult tissues.

RESULTS

Combined inactivation of *Atm* and *Hus1* results in synthetic lethality

To elucidate the genetic relationships between the ATM- and ATR-mediated DNA damage checkpoint pathways, we generated mice defective for both. Interbreeding of mice bearing targeted *Atm* and *Hus1* alleles was performed in order to produce *Atm*-deficient mice with incremental reductions in

Table 1. Synthetic lethality following combined impairment of *Hus1* and *Atm* in mice^a

<i>Hus1</i> genotype	<i>Atm</i> genotype	Number expected	Number observed
+/+	+/+	3	5
+/ <i>neo</i>		95	108
+/ <i>Δ1n</i>		12	9
<i>neo/neo</i>		259	286
<i>neo/Δ1n</i>		69	58
+/+	+/-	6	5
+/ <i>neo</i>		190	208
+/ <i>Δ1n</i>		24	31
<i>neo/neo</i>		518	659
<i>neo/Δ1n</i>		138	190
+/+	-/-	3	4
+/ <i>neo</i>		95	93
+/ <i>Δ1n</i>		12	13
<i>neo/neo</i>		259	84
<i>neo/Δ1n</i>		69	0
TOTAL		1753	1753

^a Mice were genotyped by PCR analysis of tail DNA at 3 weeks of age. Expected values represent the combined Mendelian ratios from several crosses involving different parental genotypes. The observed and expected genotype frequencies were significantly different ($P < 0.001$; χ^2 test).

Hus1 gene dosage (*Hus1*^{+/+} > *Hus1*^{+/neo} > *Hus1*^{+/Δ1n} > *Hus1*^{neo/neo} > *Hus1*^{neo/Δ1n}). *Hus1*^{+/neo} cells and mice are phenotypically normal and frequently used as wild-type equivalents in this study (14). Of the 1753 weaned offspring analyzed, no *Hus1*^{neo/Δ1n}*Atm*^{-/-} mice were obtained, and only 84 *Hus1*^{neo/neo}*Atm*^{-/-} mice were obtained, although 259 were expected (Table 1; $P < 0.001$, χ^2 test). The nature of the lethal phenotype associated with combined *Atm* and *Hus1* inactivation was determined by analyzing double-mutant and control embryos from embryonic day E8.5 to birth (Supplementary Material, Table S1). Although *Hus1*^{neo/Δ1n}*Atm*^{-/-} embryos appeared normal at E8.5, they were smaller relative to their littermates at E9.5 and all died between E10.5 and E11.5 (Fig. 1A–D). A less severe *Hus1* defect in *Hus1*^{neo/neo}*Atm*^{-/-} embryos resulted in no gross abnormalities prior to E13.5, at which point the double-mutant embryos were smaller than their littermates. Approximately 30% of *Hus1*^{neo/neo}*Atm*^{-/-} embryos were abnormal at E14.5 and died by E15.5 (Fig. 1E–H). *Hus1*^{neo/neo}*Atm*^{-/-} mice that survived beyond this mid-gestational period were significantly smaller than control littermates (Fig. 3A and B; $P < 0.05$, Student's *t*-test), and 30–40% of mice of this genotype died on the first day of life (P1) (Supplementary Material, Table S1), whereas the remainder survived beyond weaning (Table 1). Together, these data indicate that although defects in *Atm* or *Hus1* individually are compatible with grossly normal development and organismal viability, simultaneous defects in *Atm* and *Hus1* cause synthetic lethality in an *Hus1* gene dosage dependent manner.

Increased genomic instability and cell death in *Atm*/*Hus1*-deficient embryos

The failure of cells to deal with replication stress and spontaneous DNA lesions can lead to impaired cell proliferation and/or survival (15). To evaluate these outcomes in *Atm*/*Hus1*

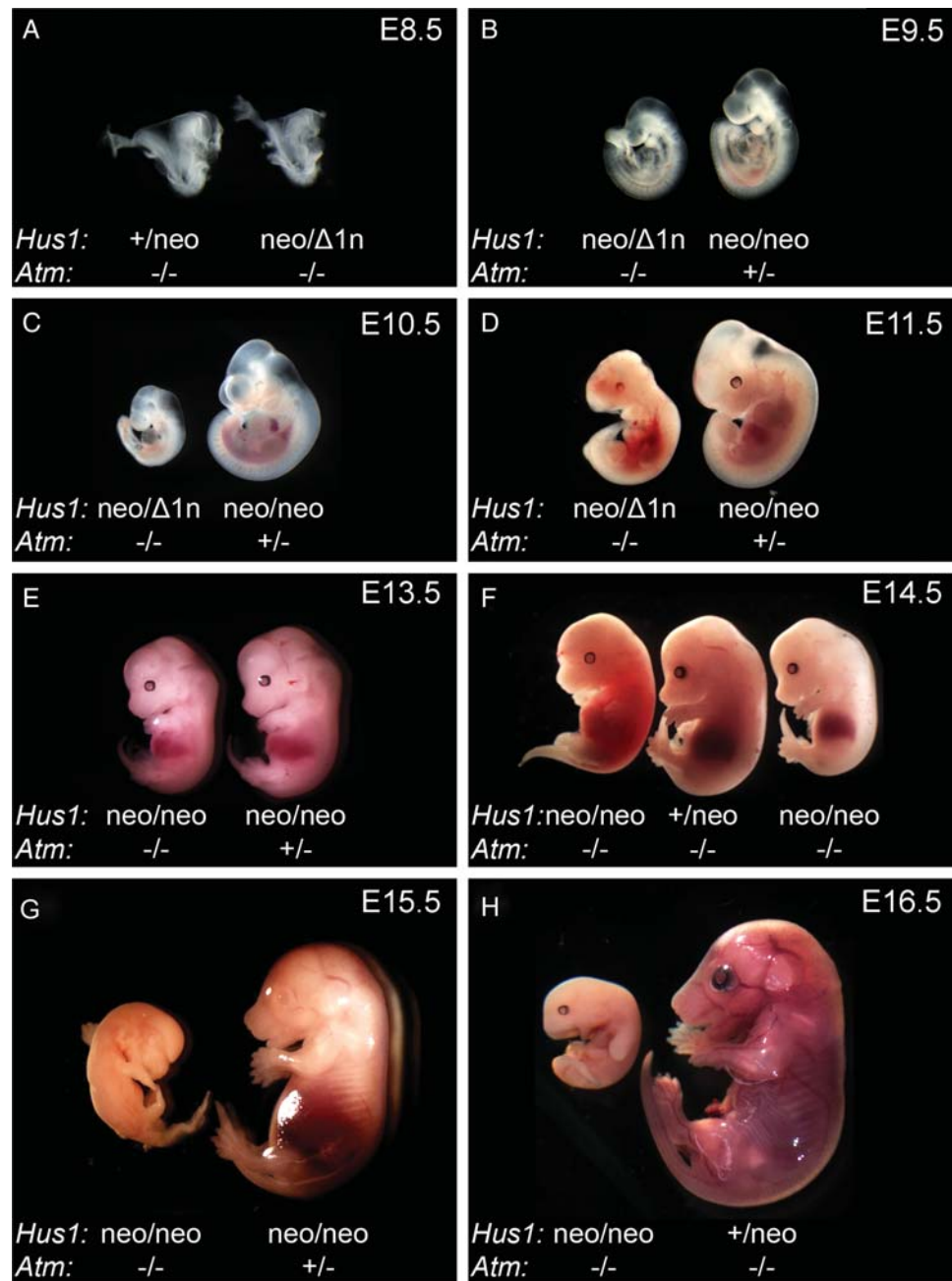


Figure 1. Embryonic lethality upon simultaneous deregulation of *Atm* and *Hus1*. Embryos from timed matings were isolated at the indicated stage of embryonic development, imaged for morphological assessment and genotyped by PCR. (A–D) Representative images of *Hus1*^{neo/Δ1n} *Atm*^{-/-} embryos and control littermates from E8.5 to E11.5. (E–H) Representative images of *Hus1*^{neo/neo} *Atm*^{-/-} embryos and control littermates from E13.5 to E16.5. Note that, at E14.5, some *Hus1*^{neo/neo} *Atm*^{-/-} embryos are dead, whereas others are smaller than control littermates but otherwise normal.

mutant embryos, we initially performed Feulgen–Schiff staining on E10.5 embryos and quantified the frequency of pyknotic and mitotic nuclei. There was a significant increase in pyknotic nuclei, indicative of apoptosis in *Hus1*^{neo/Δ1n} *Atm*^{-/-} and *Hus1*^{neo/neo} *Atm*^{-/-} embryos when compared with the *Hus1*^{+/neo} *Atm*^{+/+} control group (Supplementary Material, Fig. S1; $P < 0.001$, Student's *t*-test). By contrast, cell proliferation was unaffected. We reasoned that the apparent increase in apoptosis in the *Atm*/*Hus1* double-mutants could be due to checkpoint activation and therefore monitored the

accumulation of phosphorylated H2AX (γ -H2AX; Supplementary Material, Fig. S1D) and total p53, markers of an activated DDR (3). Terminal uridine deoxynucleotidyl transferase dUTP nick-end labeling (TUNEL) staining also was performed to directly measure apoptosis. Although almost no γ -H2AX, p53 or TUNEL-positive cells were detected in *Atm* or *Hus1* single-mutant embryos, *Hus1*^{neo/neo} *Atm*^{-/-} and, to an even greater extent, *Hus1*^{neo/Δ1n} *Atm*^{-/-} littermates showed significantly increased positive staining (Fig. 2A and B; $P < 0.05$, Student's *t*-test). Because p53 can induce cell

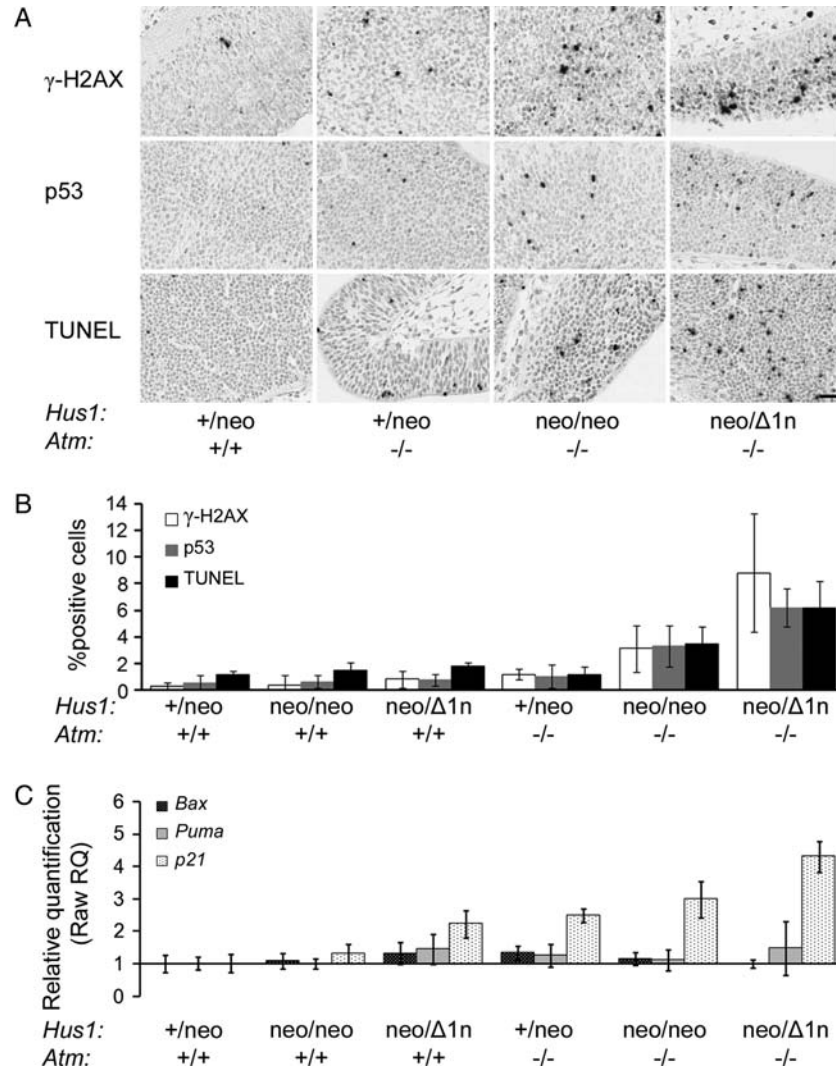


Figure 2. Significantly increased apoptosis and DDR activation in *Atm/Hus1* double-mutant embryos. Sections of E10.5 *Atm/Hus1* embryos of the indicated genotypes were stained for γ -H2AX, for p53 or by TUNEL assay. (A) Representative images of embryo neural tube sections stained for γ -H2AX, p53 and TUNEL are shown. The scale bar represents 25 μ m. (B) The percentage of γ -H2AX, TUNEL or p53-positive cells. Values are the mean of at least three embryos per genotype; error bars indicate standard deviation. Quantification was performed in the neural ectoderm to ensure that equivalent cell populations were compared between genotypes; however, similar staining patterns were observed throughout the embryos, irrespective of the cell type. The percentage of positively stained cells in *Hus1*^{neo/Δ1n}*Atm*^{-/-} and *Hus1*^{neo/neo}*Atm*^{-/-} embryos was significantly different from each other ($P < 0.05$, Student's *t*-test) and when each was compared with all the other genotypes ($P < 0.01$, Student's *t*-test). (C) The bar graph representing the fold increase in the expression level of *p21*, *Bax* and *Puma* for the embryos of the indicated genotype relative to *Hus1*^{+neo}*Atm*^{+/+} as measured by qPCR. *p21* expression was significantly increased in *Hus1*^{neo/Δ1n}*Atm*^{+/+}, *Hus1*^{+neo}*Atm*^{-/-}, *Hus1*^{neo/neo}*Atm*^{-/-} and *Hus1*^{neo/Δ1n}*Atm*^{-/-} embryos ($P < 0.05$, Student's *t*-test) and was significantly greater in *Hus1*^{neo/Δ1n}*Atm*^{-/-} embryos when compared with all other genotypes ($P < 0.05$, Student's *t*-test).

cycle arrest through transcriptional activation of *p21* or apoptosis by upregulating *Bax* and *Puma*, we used real-time PCR to measure the expression level of these genes in E10.5 embryos. Consistent with the observation of p53 accumulation in *Atm/Hus1* double-mutant embryos, there was a corresponding significant increase in *p21* expression (Fig. 2C; $P < 0.05$, Student's *t*-test). Interestingly, there were no detectable changes in *Bax* or *Puma* expression, raising the possibility of a p53-independent apoptotic mechanism. Similar results were observed by northern blot analysis (data not shown). Altogether, these findings suggest that the embryonic lethality following combined deregulation of *Atm* and *Hus1* is associated with a generalized accumulation of genome damage, activation of a DDR and ultimately widespread apoptosis.

Dwarfism in adult *Hus1*^{neo/neo}*Atm*^{-/-} mice

Approximately one-third of *Hus1*^{neo/neo}*Atm*^{-/-} mice survived to adulthood, and without exception these animals exhibited a striking dwarfism that became apparent at approximately E13.5 and persisted through adulthood (Fig. 3A–D). Consistent with previous reports (11–13), modestly reduced body size was observed in *Hus1*^{+neo}*Atm*^{-/-} mice defective for *Atm* alone. This phenotype was significantly enhanced in *Hus1*^{neo/neo}*Atm*^{-/-} animals, which on average were 40% smaller by weight than control littermates at 6 weeks of age (Fig. 3D; $P < 0.01$, mixed model analysis). Most organs were proportionally smaller in both *Hus1*^{+neo}*Atm*^{-/-} and *Hus1*^{neo/neo}*Atm*^{-/-} mice when compared with *Hus1*^{+/+}

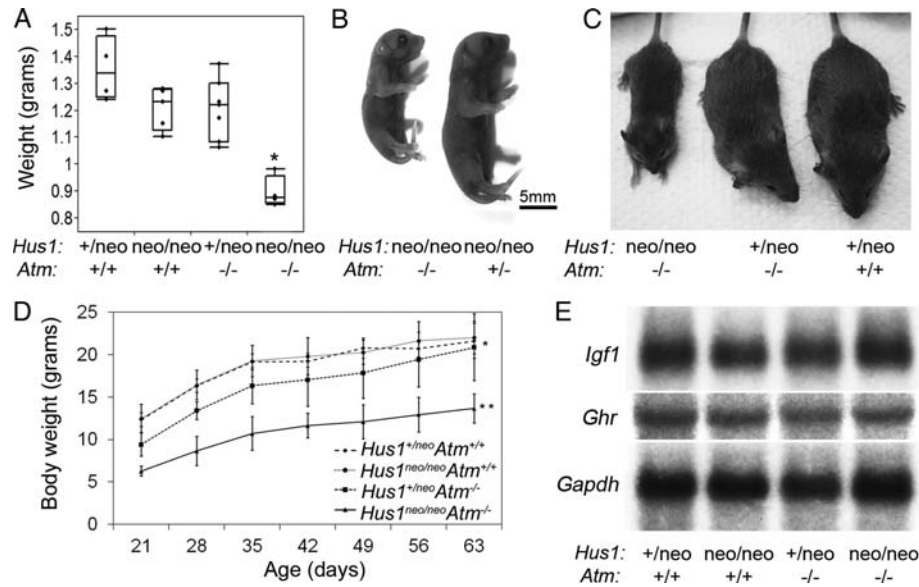


Figure 3. Dwarfism in *Hus1^{neo/neo} Atm^{-/-}* embryos and adult mice. (A) The box plot indicates the body weight of E18.5 embryos of the indicated genotypes ($n \geq 4$ per group). *Hus1^{neo/neo} Atm^{-/-}* embryos were significantly smaller than their littermates ($P < 0.001$, Student's *t*-test). (B) A representative image of newborn (P1) littermates of the indicated genotypes is shown. The scale bar represents 5 mm. (C) The photograph of 6-week-old male littermates of the indicated genotypes. (D) Body weight analysis of *Hus1^{neo/neo} Atm^{-/-}* mice and control littermates. The average body weights of female mice ($n \geq 5$ per genotype) of the indicated genotypes, from weaning to 9 weeks of age, are shown. The mean body weight was significantly lower for *Hus1^{+/neo} Atm^{-/-}* mice when compared with the *Atm^{+/+}* groups ($*P < 0.05$, mixed model analysis); *Hus1^{neo/neo} Atm^{-/-}* mice had significantly lower mean body weight when compared with all other groups ($**P < 0.01$, mixed model analysis). (E) Northern blot analysis of transcript levels of *Igf1* and *Ghr* in total RNA from the liver. *Gapdh* was used as a loading control.

Atm^{+/+} controls (Supplementary Material, Table S2). *Hus1^{neo/neo} Atm^{-/-}* mice showed a slight increase in relative brain size when compared with mice of all other genotypes, but this was not associated with any apparent histopathological abnormalities (Supplementary Material, Fig. S2).

It is well established that the somatotroph axis that includes growth hormone (GH) and insulin-like growth factor 1 (IGF1) plays important roles in somatic growth and aging (16). Deficiencies in the GH/IGF1 somatotroph axis are observed in some mouse mutants that display dwarfism in conjunction with underlying DDR defects (17). In order to understand the molecular basis for the dwarfism in *Atm/Hus1* mutant mice, we analyzed the expression levels of *Igf1* and *Ghr* and found no difference in their transcript levels in livers of 6-week-old mice of representative genotypes (Fig. 3E), findings that were confirmed by qPCR (data not shown). Furthermore, preliminary analyses revealed no differences in circulating IGF1 levels in *Hus1^{neo/neo} Atm^{-/-}* mice relative to controls (data not shown). Overall, these results demonstrate that combined *Atm* and *Hus1* deficiency has a severe impact on body size from mid-gestation to adulthood and that this proportional dwarfism arises independently of detectable abnormalities in the somatotroph axis.

Skeletal abnormalities in *Hus1^{neo/neo} Atm^{-/-}* mice

Visual inspection of *Hus1^{neo/neo} Atm^{-/-}* mice also revealed fronto-parietal alopecia and an abnormal facial morphology (Fig. 3C). To understand the origins of these abnormalities, we performed Alizarin red/Alcian blue staining of embryos. At E18.5, *Hus1^{neo/neo} Atm^{-/-}* embryos had widely open sagittal (midline) sutures and presented an array of fenestrations

primarily in the parietal bone (Fig. 4A) that were also apparent as early as E15.5 (Supplementary Material, Fig. S3A). In order to characterize the craniofacial defects in adult animals, we first produced isolated skull preparations from mice at 6 weeks of age. Grossly, *Hus1^{neo/neo} Atm^{-/-}* skulls showed a domed morphology with an incomplete closure of the sagittal sutures and reduced bone thickness in the fronto-parietal region, and multiple fenestrations in the parietal bone and jagged coronal (fronto-parietal) sutures (Fig. 4B and C). To identify and quantify patterns in skull morphology, we analyzed high-resolution three-dimensional images generated by micro-computed tomography (micro-CT) (Supplementary Material, Fig. S3D). A series of measurements were then subjected to principal component (PC) analysis to identify suites of changes in skull morphology. The first PC explained 83.6% of the total variation in the 23 skull measurements. Therefore, in a single value PC1 quantified the great majority of the skeletal variation between *Hus1^{neo/neo} Atm^{-/-}* samples and those of *Hus1^{+/neo} Atm^{+/+}*, *Hus1^{neo/neo} Atm^{+/+}* and *Hus1^{+/neo} Atm^{-/-}* genotypes (Supplementary Material, Fig. S3E). The correlations or factor loadings between the PC1 score and each distance measured for each mouse further resolved the pattern of variation: the skulls of *Hus1^{neo/neo} Atm^{-/-}* mice were smaller overall and differed in shape, with an elongated inter-parietal bone and a wider frontal bone, which increased the inter-orbital distance (Supplementary Material, Fig. S3F).

Detailed analysis of the embryonic skeletal preparations also revealed brachymesophalangy of the fifth digit (Supplementary Material, Fig. S3B and C). Interestingly, this and the related phenotype of clinodactyly are associated with several hereditary GIN syndromes, other congenital disorders

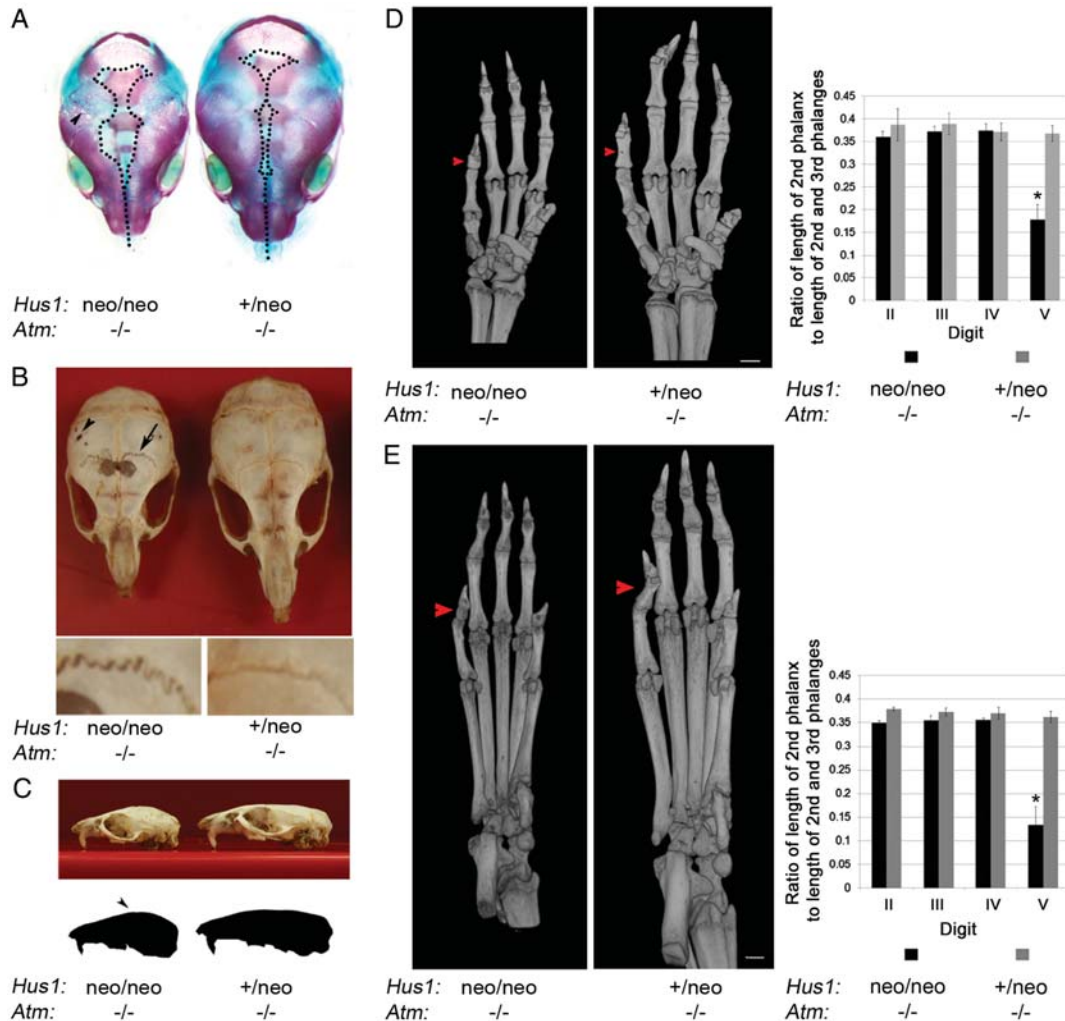


Figure 4. Skeletal abnormalities in *Hus1*^{neo/neo} *Atm*^{-/-} embryos and adult mice. (A) Shown is a representative image of Alizarin red–Alcian blue-stained skulls from E18.5 littermates of the indicated genotypes. Dotted lines outline the region where the skull plates have yet to fill in and fuse. The arrowhead indicates the fenestrations present in the *Hus1*^{neo/neo} *Atm*^{-/-} skull. (B) Skulls were prepared from 6-week-old littermates of the indicated genotypes and photographed. The arrowhead indicates the fenestrations present in the parietal bone. The arrow indicates abnormal sutures of the mutant. Lower panels: higher magnification view of sutures in the *Hus1*^{neo/neo} *Atm*^{-/-} (left) and *Hus1*^{+/neo} *Atm*^{-/-} (right) skulls. (C) A representative image of the skulls from 6-week-old littermates of the indicated genotypes is shown. The outline was generated in Adobe Photoshop to illustrate the doming of the skull. (D and E) 3D reconstructions based on micro-CT data for forelimbs (D) or hindlimbs (E) from *Hus1*^{neo/neo} *Atm*^{-/-} and *Hus1*^{+/neo} *Atm*^{-/-} mice, and the bar graphs of the corresponding measurement data ($n = 3$ per genotype). Red arrowheads point to the mesophalanx of digit V. The relative length of mesophalanx V in both forelimbs and hindlimbs was significantly shorter in *Hus1*^{neo/neo} *Atm*^{-/-} mice when compared with all other genotypes ($*P < 0.001$, Student's *t*-test).

and fetal teratogen exposure (18). Further inspection of micro-CT images indicated that the phalangeal defect was fully penetrant in adult *Hus1*^{neo/neo} *Atm*^{-/-} mice and affected both the forelimbs and hindlimbs (Fig. 4D and E). Quantitative measurements showed that the mesophalanx of the fifth digit was less than one-half of the expected size in *Hus1*^{neo/neo} *Atm*^{-/-} mice relative to controls, whereas the remaining digits were unaffected ($P < 0.001$, Student's *t*-test). Considered together with the craniofacial defects described above, these results demonstrate an essential dual function for *Atm* and *Hus1* in the development of the skeleton and suggest a potential elevated sensitivity of particular bone progenitor cells to checkpoint impairment and genomic instability.

Increased genomic instability in adult mice defective for both *Atm* and *Hus1*

HUS1 and ATM are integral components of DNA damage signaling pathways that function to protect genomic integrity. We therefore tested the impact of combined *Atm* and *Hus1* defects on GIN in adult mice by measuring micronucleus (MN) formation in peripheral blood cells, using a flow cytometry-based assay. MN are entire chromosomes or fragments of chromosomes that have not been incorporated in the main nuclei at cell division and are a hallmark of GIN. Consistent with previous findings (14,19), a moderate *Hus1* defect alone in *Hus1*^{neo/neo} *Atm*^{+/+} mice caused no significant change in MN formation relative to *Hus1*^{+/neo} *Atm*^{+/+} littermate controls,

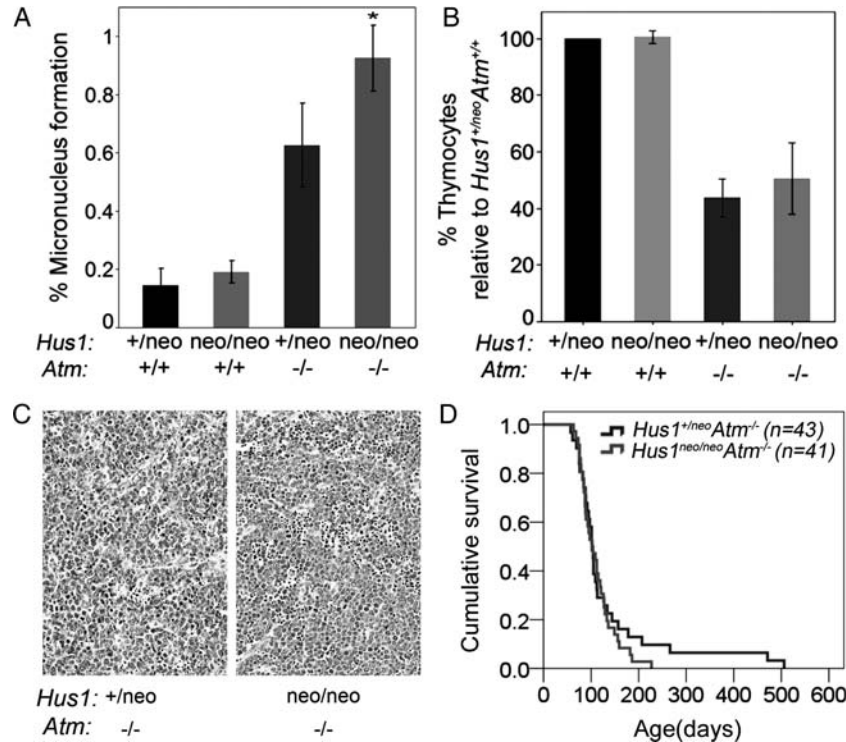


Figure 5. Increased genomic instability with no change in tumor predisposition in *Hus1^{neo/neo} Atm^{-/-}* mice. (A) The bar graph shows the average percentage of peripheral blood cells with MN in mice of the indicated genotypes. *Hus1^{+/neo} Atm^{+/+}* and *Hus1^{+/neo} Atm^{-/-}* mice showed similar levels of GIN, whereas *Hus1^{+/neo} Atm^{-/-}* mice had a significant increase in MN formation ($P < 0.001$, Student's *t*-test). The combined effect of *Hus1* impairment in an *Atm* null background (*Hus1^{neo/neo} Atm^{-/-}*) resulted in a greater than additive increase in GIN ($P = 0.002$, univariate analysis of variance). (B) The bar graph shows the relative number of thymocytes in 6-week-old mice of the indicated genotypes ($n \geq 3$ per group) expressed as a percentage of the value for *Hus1^{+/neo} Atm^{+/+}* control littermates. Error bars indicate standard deviation. The entire thymus from each mouse was harvested and mechanically disrupted, and viable trypan-blue-negative thymocytes were counted using a hemocytometer. The relative number of thymocytes was significantly lower for both *Hus1^{+/neo} Atm^{-/-}* and *Hus1^{neo/neo} Atm^{-/-}* mice ($*P < 0.001$, Student's *t*-test). (C) Representative hematoxylin and eosin-stained sections of thymic lymphomas from *Hus1^{+/neo} Atm^{-/-}* (left) and *Hus1^{neo/neo} Atm^{-/-}* (right) mice. The scale bar represents 50 μ m. (D) Cohorts of *Hus1^{+/neo} Atm^{-/-}* ($n = 41$) and *Hus1^{neo/neo} Atm^{-/-}* ($n = 43$) mice were monitored for tumor development as described in Materials and Methods. A Kaplan–Meier survival curve is shown. Overall survival was not significantly different between genotypes ($P = 0.644$, log-rank test).

whereas *Atm* deficiency alone was associated with significantly increased MN formation in *Hus1^{+/neo} Atm^{-/-}* mice (Fig. 5A; $P < 0.001$, Student's *t*-test). Notably, *Hus1^{neo/neo} Atm^{-/-}* mice had more than an additive increase in MN formation when compared with *Hus1^{neo/neo} Atm^{+/+}* and *Hus1^{+/neo} Atm^{-/-}* animals ($P = 0.002$, univariate analysis of variance). In contrast, expression of damage-inducible genes such as *p21* was unaltered in the adult liver, a relatively quiescent tissue (Supplementary Material, Fig. S4). These observations suggest that phenotypes associated with combined *Atm* and *Hus1* defects in adult mice may be more pronounced in proliferating cell populations such as blood cell precursors and highlight a potential role for replication stress as a key factor in the observed genetic interaction.

Increased GIN may influence different steps *en route* to carcinogenesis, including tumor initiation and progression, and in *Atm*-null mice contributes to the development of thymic lymphoma with near-complete penetrance (11–13). Prior to tumor development, *Hus1^{neo/neo} Atm^{-/-}* and *Hus1^{+/neo} Atm^{-/-}* mice contained similar numbers of lymphocytes in the thymus (Fig. 5B) and circulating blood (Supplementary Material, Table S3) and subsequently showed no significant difference in tumor-free survival as determined by Kaplan–Meier survival analysis (Fig. 5D). Furthermore, the resulting

neoplasms were indistinguishable histopathologically (Fig. 5C). Together, these results reveal that combined defects in *Atm* and *Hus1* result in synergistic increases in GIN in adult mice but without major consequences on thymic tumorigenesis.

Partial *Hus1* impairment synergizes with *Atm* deficiency to accelerate senescence without detectably altering key DNA damage checkpoint signaling events or radiation sensitivity

The strong genetic interaction observed between *Atm* and *Hus1* raised the possibility of overlapping roles for these checkpoint proteins in DNA damage signaling. Complete *Hus1* inactivation results in impaired activation of the ATR substrate CHK1 but does not diminish the induction of the ATM substrates CHK2 or p53 (20). Consistent with the prevailing view that ATM activation occurs independently of the 911 complex, we observed that IR- or UV-induced ATM phosphorylation occurred to a similar or greater extent in *Hus1*-null cells when compared with *Hus1*-proficient controls (Fig. 6A). To better understand the relationship between *Atm* and *Hus1* at the cell and molecular levels, we isolated primary mouse embryonic fibroblasts (MEFs) from the *Atm*/*Hus1* mouse model and analyzed their behavior in culture.

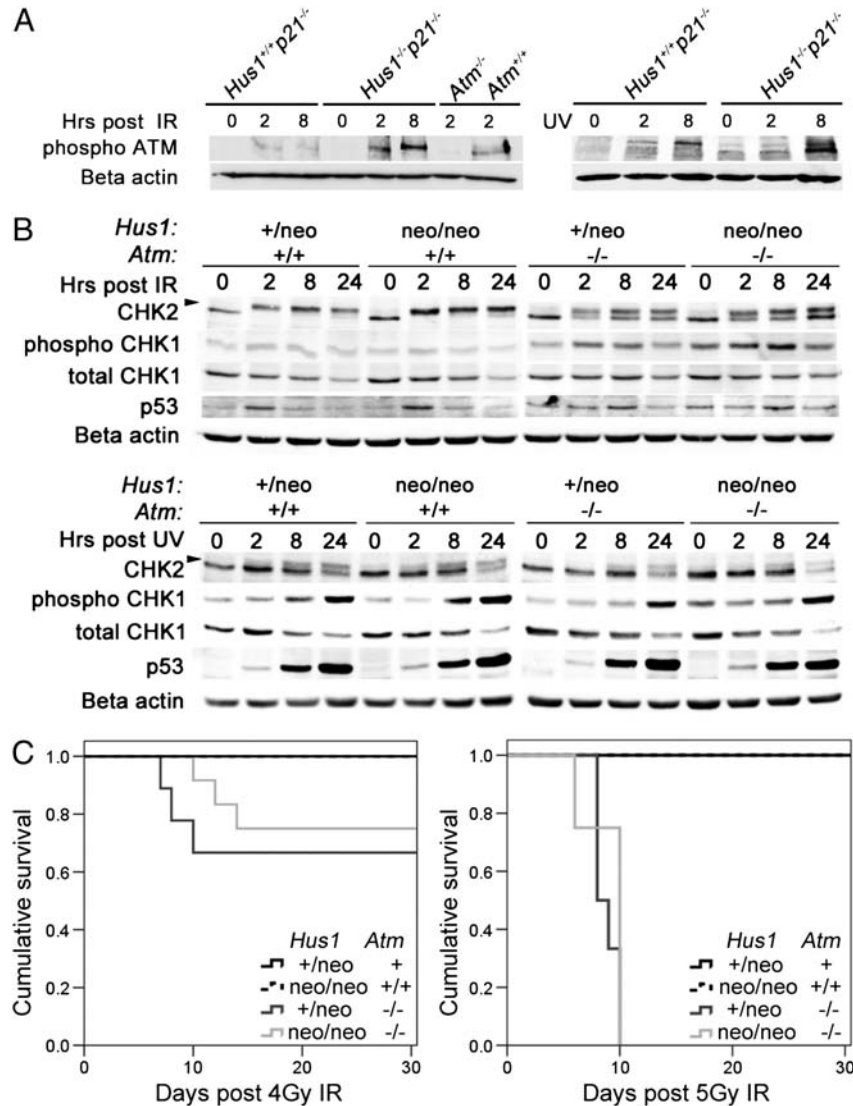


Figure 6. DNA damage signaling in *Atm/Hus1* double-mutant MEFs. (A) Immortalized MEFs of the indicated genotypes were treated with 20 Gy IR or 65 J/m² UV, and total protein lysates were prepared at 0, 2 and 8 h post-treatment. Samples were immunoblotted using antibodies specific for phospho-Ser1981-ATM, or beta-actin as a loading control. Similar results were obtained with an independent set of *Hus1*^{-/-} p21^{-/-} and matched control *Hus1*^{+/+} p21^{-/-} MEFs (data not shown). (B) Primary MEFs at passage 1 or 2 were treated with 30 Gy IR or 65 J/m² UV, and total cell protein lysates were prepared at 0, 2, 8 and 24 h post-treatment and immunoblotted for CHK1, phosphoSer345-CHK1, CHK2 and p53. The arrow indicates the position of phosphorylated CHK2. Beta-actin was used as a loading control. (C) Kaplan–Meier survival curves show the radiation sensitivity of mice of the indicated genotypes, following exposure to 4 Gy (left) or 5 Gy (right) IR. The cohort treated with 4 Gy included *Hus1*^{+/neo} *Atm*^{+/+} (*n* = 7; *Atm*^{+/+} is a combination of *Atm*^{+/+} and *Atm*^{+/-}), *Hus1*^{neo/neo} *Atm*^{+/+} (*n* = 6), *Hus1*^{+/neo} *Atm*^{-/-} (*n* = 9) and *Hus1*^{neo/neo} *Atm*^{-/-} (*n* = 12) mice. The cohort treated with 5 Gy included *Hus1*^{+/neo} *Atm*^{+/+} (*n* = 4), *Hus1*^{neo/neo} *Atm*^{+/+} (*n* = 6), *Hus1*^{+/neo} *Atm*^{-/-} (*n* = 6) and *Hus1*^{neo/neo} *Atm*^{-/-} (*n* = 4) mice. There were no significant differences in survival between *Hus1*^{+/neo} *Atm*^{-/-} and *Hus1*^{neo/neo} *Atm*^{-/-} mice after 4 Gy (*P* = 0.295) or 5 Gy (*P* = 0.366) as determined by the log-rank test.

Metaphase chromosome analysis of the MEF cultures at passage 1 revealed an increased frequency of chromosomal abnormalities in *Hus1*^{neo/neo} *Atm*^{-/-} double-mutant cells when compared with *Atm* or *Hus1* single mutants (Supplementary Material, Fig. S5). In particular, *Hus1*^{neo/neo} *Atm*^{-/-} cells exhibited a significant increase in the occurrence of extensive chromosomal damage (*P* < 0.02, Student's *t*-test) as well as an increased frequency of radial figures (*P* < 0.03, Student's *t*-test) when compared with cells of all other genotypes analyzed.

Consistent with previous results (14,21), *Atm*-deficient *Hus1*^{+/neo} *Atm*^{-/-} MEFs underwent senescence prematurely, whereas *Hus1*^{neo/neo} *Atm*^{+/+} MEFs doubled in a manner

similar to *Hus1*^{+/neo} *Atm*^{+/+} control cells. The combination of *Atm* and *Hus1* defects in *Hus1*^{neo/neo} *Atm*^{-/-} MEFs resulted in extremely rapid senescence after just a few doublings (Supplementary Material, Fig. S6A). Nevertheless, cells of all genotypes were capable of undergoing spontaneous immortalization, after which they doubled at similar rates when maintained under standard 3T3 culture conditions, both in low (3%) (data not shown) and normal (20%) O₂ levels (Supplementary Material, Fig. S6A). The proliferative capacity of the spontaneously immortalized *Atm/Hus1* MEFs was analyzed under more stringent conditions by plating cells at low density and assessing the colony-forming potential of each

cell line. Colony formation was reduced in immortalized *Hus1^{neo/neo}Atm^{+/+}* cells and impaired to an even greater degree in *Hus1^{+/neo}Atm^{-/-}* MEFs. Remarkably, *Hus1^{neo/neo}Atm^{-/-}* MEFs were completely defective for colony formation, under either atmospheric (Supplementary Material, Fig. S6B) or low-oxygen conditions (data not shown), despite the fact that these cells showed normal proliferation when cultured at higher densities. Thus, simultaneous defects in *Atm* and *Hus1* result in accelerated senescence and, despite being compatible with spontaneous immortalization, cause profound impairment of the capacity of single cells to grow out as colonies.

To further understand the cooperative relationship between ATM and HUS1 in DNA damage signaling, we next treated the *Atm/Hus1* primary MEFs with UV or IR and assessed the activation of canonical ATM and ATR downstream targets. Untreated *Hus1^{neo/neo}Atm^{-/-}* MEFs had slightly higher basal levels of p53 and phospho-CHEK1 (Fig. 6B), suggestive of increased spontaneous DNA damage accumulation. Moderate *Hus1* impairment alone had no detectable effect on DNA damage signaling upon IR treatment, with comparable levels of CHEK2 phosphorylation and p53 accumulation occurring in *Hus1^{+/neo}Atm^{+/+}* and *Hus1^{neo/neo}Atm^{+/+}* cells. The slight accumulation of phosphorylated CHEK1 following IR also was unchanged in *Hus1^{neo/neo}Atm^{+/+}* cells. Lacking ATM alone, *Hus1^{+/neo}Atm^{-/-}* cells showed delayed induction of both CHEK2 and p53 following IR and a slight increase in CHEK1 phosphorylation. Interestingly, *Hus1^{neo/neo}Atm^{-/-}* MEFs showed the same IR-induced DDR kinetics as *Hus1^{+/neo}Atm^{-/-}* cells, and the magnitude of the response was similar with the exception that CHEK1 activation after IR was even greater in cells defective for both *Atm* and *Hus1*. In response to UV, CHEK2 and CHEK1 phosphorylation as well as p53 accumulation were unaffected by *Atm* inactivation, partial *Hus1* impairment, or both (Fig. 6B). Although defects in other signaling events not analyzed here cannot be ruled out, these data suggest that primary *Atm/Hus1* double-mutant cells can trigger key DNA damage checkpoint signaling events as well as the single mutants. As a final measure of how interactions between *Atm* and *Hus1* affect the DDR, we compared the radiation sensitivity of mice with individual or combined defects in *Atm* and *Hus1*. Consistent with the lack of detectable synergistic effects on IR-induced checkpoint signaling in MEFs, *Atm/Hus1* double-mutant mice showed an equivalent sensitivity to whole-body IR exposure as *Atm* single-mutant mice, which are hypersensitive to IR (Fig. 6C). Thus, the defective DSB response in *Atm*-deficient mice is not substantially worsened by additional partial *Hus1* impairment.

DISCUSSION

The ATM and ATR DNA damage checkpoint pathways were initially viewed as separable, parallel signaling cascades that respond to distinct DNA lesions. However, recent biochemical evidence indicating significant crosstalk between the two pathways has led to the concept of a broad, integrated DDR network (22). Nevertheless, the genetic relationship between these pathways in vertebrates has been difficult to investigate due to the lethality associated with a complete inactivation of

ATR pathway components. Here we used a system for partial *Hus1* inactivation to show for the first time that ATM and HUS1 cooperate in genome maintenance *in vivo*. Whereas mice defective for either *Atm* or *Hus1* alone are viable, simultaneous dysfunction of both genes resulted in synthetic lethality. The ability to fine-tune *Hus1* expression levels further revealed tissue-specific phenotypes, such as craniofacial and limb defects, associated with moderate *Hus1* impairment in an *Atm*-deficient background. This was unexpected, as the two main mammalian DDR pathways are often considered ubiquitously important, and suggests that there is significant tissue-specific variation in the level of endogenous DNA damage and/or the activity of additional pathways that respond to DNA lesions. Mapping out these specificities will be critical for understanding the etiology of many inborn diseases as well as the nature of organismal responses to chemotherapeutics and other genotoxic agents.

The most striking phenotype in *Hus1^{neo/neo}Atm^{-/-}* mice was their significantly reduced overall size, which was apparent prior to birth. In mice and humans, there are several reports of dwarfism associated with DDR defects, but the underlying mechanisms are still poorly understood in many cases. Most theories on how DDR dysfunction causes dwarfism center on either cell-autonomous defects or systemic growth axis perturbations. In particular, the impairment of nucleotide excision repair in mouse models of Cockayne syndrome results in dwarfism, which is associated with the suppression of the GH/IGF1 axis in what is believed to represent a homeostatic feedback response to GIN (17). Likewise, SIRT6 deficiency in mice results in genomic instability, reduced *Gh/Igf1* expression and dwarfism (23). Conversely, other mouse models in which inactivation of genome maintenance mechanisms leads to dwarfism maintain an intact somatotroph axis. For instance, *Atm*-null mice are slightly smaller than their littermates (11–13) but show no differences in the circulating levels of GH or free IGF1 (24). Similarly, mice lacking KU80, a subunit of the DNA–PK complex, are smaller than their littermates but have an intact somatotroph axis (25,26).

Notably, proportional dwarfism is a characteristic of humans with Seckel syndrome. Clinical reports indicate that the GH/IGF1 axis is normal in Seckel patients, although an *Atr*-Seckel mouse model shows reduced *Igf1* and *Ghr* expression (27,28). Interestingly, Seckel syndrome also can be caused by mutations in genes encoding centrosomal proteins, including *PCNT*, *CEP152* and *CENPJ* (29–32). In these cases, defective cell division has been hypothesized to drive the cell loss that underlies the reduced body size. The apparently normal GH/IGF1 axis in *Atm/Hus1* mice suggests that a cell-autonomous defect also might be responsible for the proportional dwarfism reported here and raises the possibility that DNA damage accumulation upon combined *Atm* and *Hus1* impairment leads to small size through defective expansion of key cell populations, either throughout the body or in specific compartments that impact body size, such as stem cell pools or developing bone growth plates (33,34).

In addition to their small size, *Atm/Hus1* double-mutant animals showed skeletal abnormalities that included incomplete ossification and aberrant architecture of the skull, as well as significant shortening of the mesophalanx of the fifth digit (brachymesophalangy V) in both forelimbs and

hindlimbs. Craniofacial defects are common in patients suffering from GIN-related disorders, including Seckel syndrome (35), Nijmegen breakage syndrome (due to *NBS1* mutations) (36) and Williams–Beuren syndrome (caused by a microdeletion at 7q11.23 that includes *RFC2*) (37). Digit abnormalities, including brachymesophalangy and clinodactyly, are frequently observed in patients with Seckel syndrome as well as another GIN disorder, Fanconi anemia (38). In addition to their association with hereditary disease, craniofacial defects and brachymesophalangy V also are present following fetal exposure to teratogens, such as alcohol (39), and may be hallmarks of excessive DNA damage during development (40). Why GIN is frequently associated with these particular developmental phenotypes is largely unknown, but may reflect a heightened stress sensitivity in certain cell types. Such a mechanism has been identified in Treacher Collins syndrome, in which the occurrence of craniofacial abnormalities has been attributed to a lower threshold of neural crest cells for stress-induced p53-dependent apoptosis (41). In *Atm/Hus1* mice, cell death triggered by increased genomic instability could potentially impact crest-derived cells required for suture maintenance, possibly explaining the retarded dorsal expansion of these roofing bones. The lateral fenestrations in *Atm/Hus1* skull bones beginning at the initial stages of bone formation suggest that early ossification is disrupted, but do not provide clues as to why these specific sites are affected. The mouse model described here will be a powerful tool for understanding cell-type-specific responses to GIN and their roles in the developmental defects observed in patients with instability syndromes.

Increased GIN in *Atm/Hus1* double-mutant mice was readily apparent during embryogenesis as well as in a tissue-specific pattern in adults, as evidenced by increased MN formation in hematopoietic cells without detectable upregulation of DNA damage-responsive genes in the liver. HUS1 loss causes chromosomal instability specifically during S-phase (42), and the observations reported here are consistent with a model in which the phenotypes associated with combined *Atm* and *Hus1* defects are due primarily to the failure of actively dividing cells to deal with replication stress. Surprisingly, the elevated GIN in *Atm/Hus1* mice did not significantly change the onset or histological characteristics of thymic lymphomas relative to those arising in mice lacking *Atm* alone. It may be that the rapid onset of lymphomas in *Atm*-null mice obscures effects associated with partial *Hus1* impairment. Alternatively, a greater level of genomic instability in *Atm/Hus1* double-mutant mice may have opposing consequences that neutralize each other, both fueling the accumulation of cancer-promoting mutations and interfering with the ability of cancer cells to withstand stress-associated malignant transformation. Finally, the absence of a difference in tumor-free survival may reflect a limited requirement for *Hus1* in this compartment. Previous studies have shown that thymocytes rely more on ATM and DNA-PK than on ATR (43), and our own work suggests that lymphocytes can tolerate *Hus1* loss better than other cell types (44–46).

Unexpectedly, although we deregulated the two primary DNA damage checkpoint pathways in the *Atm/Hus1* mouse model and observed clear phenotypic consequences, we detected only limited alterations in canonical ATM/ATR-

mediated DNA damage signaling events when compared with those in *Atm* mutants alone. Indeed, for some of the factors analyzed, DNA damage signaling was increased in *Atm/Hus1* embryos and MEFs. There are several possible explanations for these observations. First, upon deregulation of the ATM and ATR pathways, an overlapping DDR kinase could become activated. Among the several possible factors that could serve such a role, the best candidate may be the PIKK DNA-PK, which is known to cooperate with ATM and ATR in H2AX phosphorylation and is capable of phosphorylating an array of DDR proteins *in vitro*, including CHK2 and p53 (47). However, CHK1 activation was readily apparent in *Atm/Hus1* double-mutants and there is limited evidence that DNA-PK phosphorylates CHK1 (48). Alternatively, ATR could mediate the checkpoint signaling either in a 911 independent manner (49) or via residual HUS1 expression from the hypomorphic *Hus1* allele. Although *Atm/Hus1*-defective cells can sense and mount signaling responses to DNA damage, this response is clearly ineffective, resulting in GIN, followed by massive apoptosis and embryonic lethality. The observed accumulation of genome damage could be due to a repair defect, an elevated damage load that overwhelms the repair machinery, or both. *Hus1* impairment did not further worsen the radiation sensitivity of *Atm*-null mice, indicating that the synthetic phenotypes in *Hus1/Atm* double-mutant mice are unlikely to originate from more severe DSB response defects relative to those in *Atm* single-mutants. Given that the 911 complex has been directly implicated in several DNA repair processes, including base excision repair and translesion synthesis, we favor the model that defective DNA repair following HUS1 deregulation leads to an increased number of DNA lesions that are normally resolved efficiently in an ATM-dependent manner, resulting in the observed synthetic lethality when both pathways are defective simultaneously (Supplementary Material, Fig. S7).

The strong genetic interaction between *Atm* and *Hus1* in mice also has implications for human disease. First, the synergistic increases in genome damage and apoptosis observed here following combined *Atm* and *Hus1* impairment suggest that therapeutic targeting of HUS1 or the broader ATR pathway may be effective for some malignancies that arise due to ATM pathway mutations, which may be as many as 70% of all cancers (50,51). However, the efficacy of such a strategy may depend on the cell of origin or other factors like the particular initiating oncogenic events in the tumor, as the impact of simultaneous *Atm* and *Hus1* defects varied between tissues. Another implication of this work relates to the basis for variant forms of A-T, like A-T_{Fresno}, which is associated with *ATM* mutations but combines typical A-T phenotypes with microcephaly and mental retardation (2). This variation has been attributed to genetic modifiers outside of *ATM*. The findings presented here suggest that polymorphisms in *HUS1* or other ATR pathway genes could significantly impact the onset and severity of A-T phenotypes.

MATERIALS AND METHODS

Animals

All animals used in this study were handled in accordance with federal and institutional guidelines, under a protocol approved

by the Cornell University Institutional Animal Care and Use Committee (IACUC). *Hus1^{neo}* and *Hus1^{ΔIn}* mice were maintained on the 129S6 background (7,14). *Atm* knockout mice were maintained on the FVB background (12). These strains were interbred to create *Atm/Hus1* double-mutant mice. Mice were genotyped by PCR analysis of genomic DNA isolated from tail snip biopsies as previously described (7). Images of live mice and skulls were taken using a Canon EOS Digital Rebel XTi digital camera equipped with a Canon EF-S 18–55 mm lens. For analysis of embryonic development, timed matings were performed. Noon of the day of vaginal plug detection was defined as embryonic day E0.5. For analysis of tumor-free survival, a cohort of mice was maintained for up to 18 months of age or until the appearance of visible neoplasms or signs of clinical disease, including weight loss, hunched posture, labored breathing, poor grooming or wasting, at which point they were euthanized by carbon dioxide asphyxiation and necropsied. For analysis of radiation sensitivity, mice were subjected to 4 or 5 Gy doses of γ -irradiation, using a Mark I Model 68 sealed ¹³⁷Cs source gamma irradiator (JL Shepherd & Associates), and monitored for up to 30 days or until reaching humane endpoint criteria based on the clinical disease signs noted above.

Histology and immunohistochemistry

Following euthanasia, isolated tissues were weighed and then fixed in 10% formalin. Embryos were fixed in 4% paraformaldehyde. Histological sections of paraffin-embedded tissues were stained with hematoxylin and eosin and subjected to pathological assessment. For the assessment of nuclear morphology, Feulgen–Schiff staining was carried out using a standard protocol (7). For immunohistochemistry, E10.5 embryos were embedded in paraffin, and serial 5 μ m sections were collected on Superfrost Plus slides (Fisher) and processed for immunohistochemistry using citric acid for p53 or EDTA for γ -H2AX-based antigen retrieval. Sections were incubated with anti- γ -H2AX (Upstate #05-636) or p53 (Cell Signaling #2524) antibodies, followed by a secondary biotinylated anti-mouse antibody (Invitrogen, Histostain SP 95-6543B). DAB (DAKO) was used as a chromogen, and hematoxylin as a counter-stain. TUNEL staining was performed using the Apoptag (Chemicon International) system according to the manufacturer's instructions. Quantification was done by counting the frequency of DAB-positive cells as depicted in Supplementary Material, Figure S1D. More than 1000 cells from at least three 100 \times fields were counted per embryo. Histology images were obtained using an Aperio Scanscope (Aperio Technologies, USA).

Skeletal morphology and measurements

Micro-CT scans were done on both living mice and isolated specimens, using GE CT120 micro-CT (GE Healthcare, London, Ontario, Canada) and Xradia VersaXRM-500 (Xradia, Pleasanton, CA, USA) scanners. Standard micro-CT scan parameters were used and are available upon request. For isolated skull preparations, mice were euthanized and decapitated, and heads were de-skinned and boiled in tap water for 20 min. Skulls were then mechanically cleaned

using forceps, whereas the brain was removed by flushing with water. Skulls were dried before being stored. For live imaging, mice were anesthetized with isoflurane and scanned. In order to accurately measure the distance between two points of interest, we developed a tool for marking points on the skull surface in three-dimensional (3D) image space. For every marked point, a surface coordinate location was computed in millimeters for *x*, *y* and *z* 3-D coordinates. The distance between any two surface points was computed using the Euclidean distance of the mapped image coordinates. Statistical analysis of the resulting morphometry data was performed by a PC analysis using the *princomp()* function and a covariance matrix in R 2.6.0. Limbs were isolated after euthanasia and subjected to micro-CT imaging as described above. Analysis of the resulting data and 3D reconstructions were done using the OsiriX software (52). Skeletal staining with Alcian blue and Alizarin red was performed as previously described (53). Briefly, embryos were eviscerated, fixed in 80% ethanol for at least 24 h, dehydrated in 95% ethanol and stained overnight with Alcian blue (Sigma A3157) in 95% ethanol:1% glacial acetic acid solution. The bone was counterstained with Alizarin red (Sigma A5533) in 2% KOH for 3 h. Embryos were cleared in a decreasing 2% KOH/glycerol series (80:20; 60:40; 40:60) for 24 h each and stored indefinitely in 2% KOH:glycerol (20:80). The stained embryos were imaged using a Leica MZ125 inverse microscope equipped with an RT slider camera (Diagnostic Instruments).

MN assay

Analysis of MN formation in peripheral blood cells was performed as previously described (14,19). Briefly, peripheral blood was collected from the mandibular vein, fixed in methanol and incubated in bicarbonate buffer containing RNase A and anti-CD71: FITC antibody (Bioscience International). After washing and staining with propidium iodide, the cells were analyzed on a FACSCalibur flow cytometer (Becton-Dickinson, San Jose, CA, USA).

Cell culture and proliferation measurements

MEFs were prepared from E13.5 embryos, following timed matings between *Hus1^{+/neo}Atm^{+/-}* and *Hus1^{neo/neo}Atm^{+/-}* mice. Briefly, embryos were dissected from the deciduum, mechanically disrupted and cultured in DMEM supplemented with 10% fetal bovine serum, 1.0 mM L-glutamine, 0.1 mM minimal essential medium nonessential amino acids, 100 μ g/ml streptomycin sulfate and 100 U/ml penicillin. The initial plating was defined as passage zero (p0), and cells were subsequently maintained on a 3T3 protocol (54). Clonogenic potential was assessed by plating MEFs in six-well dishes at 5×10^2 or 3×10^3 cells per well and changing the media every 3 days. After 11 days in culture, cells were washed with PBS and fixed in methanol for 1 h at room temperature, stained overnight with a 5% crystal violet solution in 70% ethanol and washed with tap water. Immortalized *Hus1^{+/+}p21^{-/-}* and *Hus1^{-/-}p21^{-/-}* MEFs were described previously (7). For IR treatment, cells at passage 2 or 3 were exposed to γ -irradiation, using a Mark I Model 68

sealed ^{137}Cs source gamma irradiator (JL Shepherd & Associates), at a dose rate of 123.1 rad/min. For UV treatment, the medium was removed from the cells, cells were washed with PBS, the top of the culture dish was removed and the cells were exposed to 254 nm UV light, using a XL-1000 UV Crosslinker (Spectro Linker).

Northern blotting and real-time PCR

Total RNA was prepared from E10.5 embryos and from the liver, using RNA STAT-60 reagent (Tel-Test, Friendswood, TX, USA), and then resolved on a 1% agarose/formaldehyde gel, transferred to a nylon membrane, and hybridized with ^{32}P -labeled cDNA probes. Quantification of signal intensity was done using a Storm 860 phosphorimager (Molecular Dynamics, Sunnyvale, CA, USA). Total RNA was used for reverse transcription, using the SuperScript III kit (Invitrogen) according to the manufacturer's instructions. Quantitative real-time PCR (q-PCR) was performed on an ABI 7500 System (PE Applied-Biosystems) using cDNA as a template in the presence of SYBR-green (Quanta Biosciences PerfeCTa SYBR Green FastMix). Primer pairs were designed using the Integrated DNA Technologies' RealTime PCR Assay Design Tool (www.idtdna.com) to generate intron-spanning products of 150–200 bp as follows: *Ghr*: 5'-AGCCTCGATTACCAAGTG-3' and 5'-AATTCTTGCACTTGTCGTTG-3'; *Igf1*: 5'-GAGACTGGAGATGTACTGTGC-3' and 5'-CTCCTTTG CAGCTTCGTTTTTC-3'; *Gstt2*: 5'-TGCCCAAGTCCACGAA TAC-3' and 5'-CCAGGACCATTCTATCTCTGTTC-3'; *Bax*: 5'-TTGGAGATGAAGTGGACAGC-3' and 5'-CAGTTGAAG TTGCCATCAGC-3'; *Puma*: 5'-CTGGAGGGTCATGTACA ATCTC-3' and 5'-GGTGTGAGAAGGCGGAG-3'; *p21*: 5'-C TTGCACTCTGGTGTCTGAG-3' and 5'-GCACTTCAGGGT TTTCTCTTG-3'; *beta-actin*: 5'-ACCTTCTACAATGAGCT GCG-3' and 5'-CTGGATGGCTACGTACATGG-3'. The generation of specific PCR products was confirmed by melting curve analysis and gel electrophoresis. Each primer pair was tested with a logarithmic dilution of cDNA mix to generate a linear standard curve, which was used to calculate the primer pair efficiency (55).

Western blotting

Cells were harvested and solubilized in RIPA buffer as described previously (56), or protein was extracted using a high-salt extraction procedure (57). Total protein was quantified by the Bradford assay, resolved on 6–14% SDS–PAGE gels and subjected to immunoblotting using antibodies from Millipore (anti- $\gamma\text{-H2AX}$, #05-636 and anti-CHK2, #05-649), Santa Cruz (anti-CHK1, G-4; sc-8408 and anti-p53, FL-393; sc-6243), Cell Signaling (anti-phospho-CHK1, Ser345, #2341), Rockland (anti-ATM, pSer1981, 200-310-400) and Sigma (anti-beta actin, #A5441). Western blot imaging and quantification were performed using a Versa Doc Imaging System (Bio-Rad Laboratories).

SUPPLEMENTARY MATERIAL

Supplementary Material is available at *HMG* online.

ACKNOWLEDGEMENTS

The authors thank Eric Alani, Sylvia Lee and Yolanda Sanchez for helpful discussions and comments on the manuscript; Yves Boisclair for measurements of circulating IGF1 levels; and the staff of the Cornell Lab Animal Services and CARE programs for excellent animal care.

Conflict of Interest statement. None declared.

FUNDING

This work was supported by National Institutes of Health grants (R01 CA108773 and R03 HD058220 to R.S.W.); a Cornell University College of Veterinary Medicine Graduate Research Assistantship to G.B.; National Institutes of Health training grant (T32 HD052471) funding to A.M.L.; a Cornell University College of Veterinary Medicine Clinical Fellowship to K.R.H.; and a National Center for Research Resources grant (S10RR023781) for instrumentation. The funders had no role in the study design, data collection and analysis, decision to publish or preparation of the manuscript.

REFERENCES

- McKinnon, P.J. (2012) ATM and the molecular pathogenesis of ataxia telangiectasia. *Annu. Rev. Pathol.*, **7**, 303–321.
- Gilad, S., Chessa, L., Khosravi, R., Russell, P., Galanty, Y., Piane, M., Gatti, R.A., Jorgensen, T.J., Shiloh, Y. and Bar-Shira, A. (1998) Genotype-phenotype relationships in ataxia-telangiectasia and variants. *Am. J. Hum. Genet.*, **62**, 551–561.
- Jackson, S.P. and Bartek, J. (2009) The DNA-damage response in human biology and disease. *Nature*, **461**, 1071–1078.
- Cimprich, K.A. and Cortez, D. (2008) ATR: an essential regulator of genome integrity. *Nat. Rev. Mol. Cell Biol.*, **9**, 616–627.
- Kemp, M. and Sancar, A. (2009) DNA distress: just ring 9-1-1. *Curr. Biol.*, **19**, R733–R734.
- Helt, C.E., Wang, W., Keng, P.C. and Bambara, R.A. (2005) Evidence that DNA damage detection machinery participates in DNA repair. *Cell Cycle*, **4**, 529–532.
- Weiss, R.S., Enoch, T. and Leder, P. (2000) Inactivation of mouse Hus1 results in genomic instability and impaired responses to genotoxic stress. *Genes Dev.*, **14**, 1886–1898.
- Hopkins, K.M., Auerbach, W., Wang, X.Y., Hande, M.P., Hang, H., Wolgemuth, D.J., Joyner, A.L. and Lieberman, H.B. (2004) Deletion of mouse rad9 causes abnormal cellular responses to DNA damage, genomic instability, and embryonic lethality. *Mol. Cell Biol.*, **24**, 7235–7248.
- O'Driscoll, M. (2009) Mouse models for ATR deficiency. *DNA Repair (Amst.)*, **8**, 1333–1337.
- O'Driscoll, M. (2008) Haploinsufficiency of DNA damage response genes and their potential influence in human genomic disorders. *Curr. Genomics*, **9**, 137–146.
- Barlow, C., Hirotsune, S., Paylor, R., Liyanage, M., Eckhaus, M., Collins, F., Shiloh, Y., Crawley, J.N., Ried, T., Tagle, D. *et al.* (1996) Atm-deficient mice: a paradigm of ataxia telangiectasia. *Cell*, **86**, 159–171.
- Elson, A., Wang, Y., Daugherty, C.J., Morton, C.C., Zhou, F., Campos-Torres, J. and Leder, P. (1996) Pleiotropic defects in ataxia-telangiectasia protein-deficient mice. *Proc. Natl Acad. Sci. USA*, **93**, 13084–13089.
- Xu, Y., Ashley, T., Brainerd, E.E., Bronson, R.T., Meyn, M.S. and Baltimore, D. (1996) Targeted disruption of ATM leads to growth retardation, chromosomal fragmentation during meiosis, immune defects, and thymic lymphoma. *Genes Dev.*, **10**, 2411–2422.
- Levitt, P.S., Zhu, M., Cassano, A., Yazinski, S.A., Liu, H., Darfler, J., Peters, R.M. and Weiss, R.S. (2007) Genome maintenance defects in

- cultured cells and mice following partial inactivation of the essential cell cycle checkpoint gene *Hus1*. *Mol. Cell. Biol.*, **27**, 2189–2201.
15. Bartek, J., Lukas, C. and Lukas, J. (2004) Checking on DNA damage in S phase. *Nat. Rev. Mol. Cell Biol.*, **5**, 792–804.
 16. Lupu, F., Terwilliger, J.D., Lee, K., Segre, G.V. and Efstratiadis, A. (2001) Roles of growth hormone and insulin-like growth factor 1 in mouse postnatal growth. *Dev. Biol.*, **229**, 141–162.
 17. Niedernhofer, L.J. (2008) Tissue-specific accelerated aging in nucleotide excision repair deficiency. *Mech. Ageing Dev.*, **129**, 408–415.
 18. Rypens, F., Dubois, J., Garel, L., Fournet, J.C., Michaud, J.L. and Grignon, A. (2006) Obstetric US: watch the fetal hands. *Radiographics*, **26**, 811–832.
 19. Shima, N., Hartford, S.A., Duffy, T., Wilson, L.A., Schimenti, K.J. and Schimenti, J.C. (2003) Phenotype-based identification of mouse chromosome instability mutants. *Genetics*, **163**, 1031–1040.
 20. Weiss, R.S., Matsuoka, S., Elledge, S.J. and Leder, P. (2002) *Hus1* acts upstream of *chk1* in a mammalian DNA damage response pathway. *Curr. Biol.*, **12**, 73–77.
 21. Xu, Y. and Baltimore, D. (1996) Dual roles of ATM in the cellular response to radiation and in cell growth control. *Genes. Dev.*, **10**, 2401–2410.
 22. Matsuoka, S., Ballif, B.A., Smogorzewska, A., McDonald, E.R. III, Hurov, K.E., Luo, J., Bakalarski, C.E., Zhao, Z., Solimini, N., Lerenthal, Y. et al. (2007) ATM and ATR substrate analysis reveals extensive protein networks responsive to DNA damage. *Science*, **316**, 1160–1166.
 23. Mostoslavsky, R., Chua, K.F., Lombard, D.B., Pang, W.W., Fischer, M.R., Gellon, L., Liu, P., Mostoslavsky, G., Franco, S., Murphy, M.M. et al. (2006) Genomic instability and aging-like phenotype in the absence of mammalian SIRT6. *Cell*, **124**, 315–329.
 24. Schubert, R., Schmitz, N., Pietzner, J., Tandi, C., Theisen, A., Dresel, R., Christmann, M. and Zielen, S. (2009) Growth hormone supplementation increased latency to tumorigenesis in *Atm*-deficient mice. *Growth Factors*, **27**, 265–273.
 25. van de Ven, M., Andressoo, J.O., Holcomb, V.B., von Lindern, M., Jong, W.M., De Zeeuw, C.I., Suh, Y., Hasty, P., Hoeijmakers, J.H., van der Horst, G. T. et al. (2006) Adaptive stress response in segmental progeria resembles long-lived dwarfism and calorie restriction in mice. *PLoS Genet.*, **2**, e192.
 26. Nussenzweig, A., Chen, C., da Costa Soares, V., Sanchez, M., Sokol, K., Nussenzweig, M.C. and Li, G.C. (1996) Requirement for Ku80 in growth and immunoglobulin V(D)J recombination. *Nature*, **382**, 551–555.
 27. Kjaer, I., Hansen, N., Becktor, K.B., Birkebaek, N. and Balslev, T. (2001) Craniofacial morphology, dentition, and skeletal maturity in four siblings with Seckel syndrome. *Cleft Palate Craniofac. J.*, **38**, 645–651.
 28. Murga, M., Bunting, S., Montana, M.F., Soria, R., Mulero, F., Canamero, M., Lee, Y., McKinnon, P.J., Nussenzweig, A. and Fernandez-Capetillo, O. (2009) A mouse model of ATR-Seckel shows embryonic replicative stress and accelerated aging. *Nat. Genet.*, **41**, 891–898.
 29. Al-Dosari, M.S., Shaheen, R., Colak, D. and Alkuraya, F.S. (2010) Novel CENPJ mutation causes Seckel syndrome. *J. Med. Genet.*, **47**, 411–414.
 30. Kalay, E., Yigit, G., Aslan, Y., Brown, K.E., Pohl, E., Bicknell, L.S., Kayserili, H., Li, Y., Tuysuz, B., Nurnberg, G. et al. (2011) CEP152 is a genome maintenance protein disrupted in Seckel syndrome. *Nat. Genet.*, **43**, 23–26.
 31. Rauch, A., Thiel, C.T., Schindler, D., Wick, U., Crow, Y.J., Ekici, A.B., van Essen, A.J., Goecke, T.O., Al-Gazali, L., Chrzanowska, K.H. et al. (2008) Mutations in the pericentrin (PCNT) gene cause primordial dwarfism. *Science*, **319**, 816–819.
 32. Griffith, E., Walker, S., Martin, C.A., Vagnarelli, P., Stiff, T., Vernay, B., Al Sanna, N., Saggat, A., Hamel, B., Earnshaw, W.C. et al. (2008) Mutations in pericentrin cause Seckel syndrome with defective ATR-dependent DNA damage signaling. *Nat. Genet.*, **40**, 232–236.
 33. Klingseisen, A. and Jackson, A.P. (2011) Mechanisms and pathways of growth failure in primordial dwarfism. *Genes. Dev.*, **25**, 2011–2024.
 34. Lui, J.C. and Baron, J. (2011) Mechanisms limiting body growth in mammals. *Endocr. Rev.*, **32**, 422–440.
 35. Goodship, J., Gill, H., Carter, J., Jackson, A., Splitt, M. and Wright, M. (2000) Autozygosity mapping of a seckel syndrome locus to chromosome 3q22.1–q24. *Am. J. Hum. Genet.*, **67**, 498–503.
 36. Digweed, M. and Sperling, K. (2004) Nijmegen breakage syndrome: clinical manifestation of defective response to DNA double-strand breaks. *DNA Repair (Amst.)*, **3**, 1207–1217.
 37. Osborne, L.R. (1999) Williams-Beuren syndrome: unraveling the mysteries of a microdeletion disorder. *Mol. Genet. Metab.*, **67**, 1–10.
 38. De Kerviler, E., Guermazi, A., Zagdanski, A.M., Gluckman, E. and Fria, J. (2000) The clinical and radiological features of Fanconi's anaemia. *Clin. Radiol.*, **55**, 340–345.
 39. Manning, M.A. and Eugene Hoyme, H. (2007) Fetal alcohol spectrum disorders: a practical clinical approach to diagnosis. *Neurosci. Biobehav. Rev.*, **31**, 230–238.
 40. Holmes, L.B., Kleiner, B.C., Leppig, K.A., Cann, C.I., Munoz, A. and Polk, B.F. (1987) Predictive value of minor anomalies: II. Use in cohort studies to identify teratogens. *Teratology*, **36**, 291–297.
 41. Jones, N.C., Lynn, M.L., Gaudenz, K., Sakai, D., Aoto, K., Rey, J.P., Glynn, E.F., Ellington, L., Du, C., Dixon, J. et al. (2008) Prevention of the neurocristopathy Treacher Collins syndrome through inhibition of p53 function. *Nat. Med.*, **14**, 125–133.
 42. Zhu, M. and Weiss, R.S. (2007) Increased common fragile site expression, cell proliferation defects, and apoptosis following conditional inactivation of mouse *Hus1* in primary cultured cells. *Mol. Biol. Cell*, **18**, 1044–1055.
 43. Callen, E., Jankovic, M., Wong, N., Zha, S., Chen, H.T., Difilippantonio, S., Di Virgilio, M., Heidkamp, G., Alt, F.W., Nussenzweig, A. et al. (2009) Essential role for DNA-PKcs in DNA double-strand break repair and apoptosis in ATM-deficient lymphocytes. *Mol. Cell*, **34**, 285–297.
 44. Francia, S., Weiss, R.S., Hande, M.P., Freire, R. and d'Adda di Fagnana, F. (2006) Telomere and telomerase modulation by the mammalian Rad9/Rad1/Hus1 DNA-damage-checkpoint complex. *Curr. Biol.*, **16**, 1551–1558.
 45. Levitt, P.S., Liu, H., Manning, C. and Weiss, R.S. (2005) Conditional inactivation of the mouse *Hus1* cell cycle checkpoint gene. *Genomics*, **86**, 212–224.
 46. Yazinski, S.A., Westcott, P.M., Ong, K., Pinkas, J., Peters, R.M. and Weiss, R.S. (2009) Dual inactivation of *Hus1* and p53 in the mouse mammary gland results in accumulation of damaged cells and impaired tissue regeneration. *Proc. Natl Acad. Sci. USA*, **106**, 21282–21287.
 47. Meek, K., Dang, V. and Lees-Miller, S.P. (2008) DNA-PK: the means to justify the ends? *Adv. Immunol.*, **99**, 33–58.
 48. Jazayeri, A., Falck, J., Lukas, C., Bartek, J., Smith, G.C., Lukas, J. and Jackson, S.P. (2006) ATM- and cell cycle-dependent regulation of ATR in response to DNA double-strand breaks. *Nat. Cell Biol.*, **8**, 37–45.
 49. Navadgi-Patil, V.M. and Burgers, P.M. (2009) A tale of two tails: activation of DNA damage checkpoint kinase Mec1/ATR by the 9-1-1 clamp and by Dpb11/TopBP1. *DNA Repair (Amst.)*, **8**, 996–1003.
 50. Shiloh, Y. (2003) ATM and related protein kinases: safeguarding genome integrity. *Nat. Rev. Cancer*, **3**, 155–168.
 51. Reaper, P.M., Griffiths, M.R., Long, J.M., Charrier, J.D., McCormick, S., Charlton, P.A., Golec, J.M. and Pollard, J.R. (2011) Selective killing of ATM- or p53-deficient cancer cells through inhibition of ATR. *Nat. Chem. Biol.*, **7**, 428–430.
 52. Rosset, A., Spadola, L. and Ratib, O. (2004) OsiriX: an open-source software for navigating in multidimensional DICOM images. *J. Digit. Imaging*, **17**, 205–216.
 53. Kaufman, M.H. (1992) *The Atlas of Mouse Development*. Academic Press, London/San Diego.
 54. Todaro, G.J. and Green, H. (1963) Quantitative studies of the growth of mouse embryo cells in culture and their development into established lines. *J. Cell Biol.*, **17**, 299–313.
 55. Dean, F., Tea, M. and Fenster, S. (2008) Real-time PCR. *Curr. Protoc. Essent. Lab. Tech.*, **UNIT 10.3**, 10.3.1–10.3.34.
 56. Harlow, E. and Lane, D. (2006) Lysing tissue-culture cells for immunoprecipitation. *Cold Spring Harb. Protoc.*, doi:10.1101/pdb.prot4531.
 57. Achari, Y. and Lees-Miller, S.P. (2000) Detection of DNA-dependent protein kinase in extracts from human and rodent cells. *Methods Mol. Biol.*, **99**, 85–97.